

The impact of baryons on the matter power spectrum from the Horizon-AGN cosmological hydrodynamical simulation

N. E. Chisari^{1*}, M. L. A. Richardson^{1,2}, J. Devriendt¹, Y. Dubois³, A. Schneider⁴, A. M. C. Le Brun^{5,6}, R. S. Beckmann^{1,3}, S. Peirani^{3,7}, A. Slyz¹, C. Pichon^{3,8}

¹Department of Physics, University of Oxford, Keble Road, Oxford, OX1 3RH, UK.

²Department of Astrophysics, American Museum of Natural History, 79th Street at Central Park West, New York, NY 10024, USA.

³Institut d’Astrophysique de Paris, CNRS & UPMC, UMR 7095, 98 bis Boulevard Arago, 75014, Paris, France.

⁴Institute for Particle Physics and Astrophysics, ETH Zurich, Wolfgang-Pauli-Strasse 27, CH-8093 Zurich, Switzerland.

⁵IRFU, CEA, Université Paris-Saclay, F-91191 Gif-sur-Yvette, France.

⁶Université Paris Diderot, AIM, Sorbonne Paris Cité, CEA, CNRS, F-91191 Gif-sur-Yvette, France.

⁷Université Côte d’Azur, Observatoire de la Côte d’Azur, CNRS, Laboratoire Lagrange, France.

⁸Korea Institute of Advanced studies (KIAS), 85 Hoegiro, Dongdaemun-gu, Seoul, 02455, Republic of Korea.

25 Jan 2018
arXiv:1801.08559v1 [astro-ph.CO]

Accepted XXXX. Received XXXX; in current form June 12, 2019

ABSTRACT

Accurate cosmology from upcoming weak lensing surveys relies on knowledge of the total matter power spectrum at percent level at scales $k < 10 \text{ h/Mpc}$, for which modelling the impact of baryonic physics is crucial. We compare measurements of the total matter power spectrum from the Horizon cosmological hydrodynamical simulations: a dark matter-only run, one with full baryonic physics, and another lacking Active Galactic Nuclei (AGN) feedback. Baryons cause a suppression of power at $k \simeq 10 \text{ h/Mpc}$ of $< 15\%$ at $z = 0$, and an enhancement of a factor of a few at smaller scales due to the more efficient cooling and star formation. The results are sensitive to the presence of the highest mass haloes in the simulation and the distribution of dark matter is also impacted up to a few percent. The redshift evolution of the effect is non-monotonic throughout $z = 0 - 5$ due to an interplay between AGN feedback and gas pressure, and the growth of structure. We investigate the effectiveness of the “baryonic correction model” proposed by Schneider & Teyssier (2015) in describing our results. We require a different redshift evolution and propose an alternative fitting function with 4 free parameters that reproduces our results within 5%. Compared to other simulations, we find the impact of baryonic processes on the total matter power spectrum to be smaller at $z = 0$. Nevertheless, our results also suggest that AGN feedback is not strong enough in the simulation. Total matter power spectra from the Horizon simulations are made publicly available at <https://www.horizon-simulation.org/catalogues.html>.

Key words: cosmology: theory — gravitational lensing: weak – large-scale structure of Universe — methods: numerical

1 INTRODUCTION

The next generation of optical galaxy surveys will rely on different proxies for the distribution of matter in the Universe to constrain its components and their evolution. One such observable is the weak gravitational lensing of galaxies, percent-level distortions of their ellipticities which are

caused by bending of the path of distant photons due to gravity, first detected by Tyson et al. (1990). These distortions can be used to map the distribution of matter in the Universe through cosmic time to set constraints on the evolution of dark energy, theories of gravity and the nature of dark matter, among other applications. For reviews of weak lensing theory, methods and applications, see Bartelmann & Schneider (2001); Weinberg et al. (2013); Kilbinger (2015).

* elisa.chisari@physics.ox.ac.uk

Previous and ongoing weak lensing surveys, such as the Sloan Digital Sky Survey (Huff et al. 2014), the Canada-France-Hawaii Telescope Lensing Survey (Heymans et al. 2012), the Kilo Degree Survey (de Jong et al. 2013), the Deep Lens Survey (Wittman et al. 2002) and the Dark Energy Survey (Troxel et al. 2017), among others, have demonstrated the feasibility and potential of this method for precision cosmology. Future experiments with better constraining power are planned or under construction, such as the Large Synoptic Survey Telescope (Ivezic et al. 2008, LSST), *Euclid* (Laureijs et al. 2011) and *WFIRST* (Green et al. 2011). To successfully extract information from weak gravitational lensing measurements from these next generation of galaxy surveys, accurate prior knowledge on the distribution of matter is required. This requirement is typically phrased in terms of knowledge of the *total matter power spectrum*, $P(k)$, which quantifies the amount of statistical power in a given Fourier mode of the matter overdensity field. For the next generation of surveys, the total matter power spectrum needs to be known to at least within 1% accuracy up to $k = 10 h/\text{Mpc}$ to achieve the desired accuracy in cosmological parameter constraints (Huterer & Takada 2005; Laureijs 2009; Hearin et al. 2012).

In the past, it was sufficient to model the total matter power spectrum via analytical techniques (e.g. Howlett et al. 2012; Takahashi et al. 2012) or using dark matter-only (DMO) simulations (e.g. Heitmann et al. 2014). Recently, van Daalen et al. (2011) demonstrated that baryonic effects can have a significant impact on the distribution of matter, which needs to be incorporated into weak lensing analysis pipelines. The main effect to model is the suppression of power at scales of a few Mpc associated with gas ejected by Active Galactic Nuclei (AGN). Cosmological hydrodynamical simulations can provide these predictions, and results from several state-of-the-art simulations are available in the literature (van Daalen et al. 2011; Vogelsberger et al. 2014; Hellwing et al. 2016; Tenneti et al. 2014; Springel et al. 2017). Such simulations differ in the numerical methods and the implementation of baryonic ('sub-grid') processes, which can in turn result in varying predictions for the total matter power spectrum at small scales, where these physical processes are relevant.

Effective analytical models to account for the impact of baryons on the total distribution of matter have also been devised. Some of these consist of modifications of the 'halo model' (Seljak 2000; Semboloni et al. 2013; Fedeli 2014; Mead et al. 2015), others of effective parameterisations of the transfer of power produced by the presence of baryons based on observational constraints and/or simulation results (Mohammed & Seljak 2014; Schneider & Teyssier 2015). Several techniques to mitigate the presence of baryons have been proposed: marginalisation over the parameters of effective models (Semboloni et al. 2011) or over the principal components in linear combinations of observables that are most strongly affected by baryonic effects (Eifler et al. 2015; Kitching et al. 2016). The success of these techniques depends on the flexibility of the models to capture the true underlying matter distribution (Mohammed & Gnedin 2017).

In this work, we present results on the impact of baryons

on the distribution of matter from the Horizon set of simulations, a state-of-the-art set of simulations with full implementation of baryonic physics (Dubois et al. 2014, 2016). The Horizon set comprises three simulations with the same volume and initial conditions. The main run includes all baryonic physics processes, a second run lacks AGN feedback and the third run is a DMO box for comparison. Horizon differs from other cosmological hydrodynamic simulations in several aspects. The numerical method implemented is based on the "adaptive-mesh-refinement" (AMR) technique and the only requirement on sub-grid parameters is such that the simulation matches the observed stellar mass-black hole mass relation and the black hole mass-velocity dispersion ($M_{\text{BH}} - \sigma$) relation at $z = 0$. The full physics run, Horizon-AGN, has been shown to be in good agreement with observations of the star formation history of the Universe, and colours and luminosity functions of galaxies across a wide range of redshifts, as shown by Kaviraj et al. (2017). These authors nevertheless identified an excess of low-mass red galaxies at low redshift, which was attributed to supernovae feedback being too inefficient in preventing the formation of these galaxies.

We quantify the impact of baryons and the role of AGN feedback on the distribution of matter across the range of scales and redshifts of interest to weak gravitational lensing surveys. We compare our results to those from other groups and we test the applicability of the baryonic correction (BC) model of Schneider & Teyssier (2015) using our results. We make tables of the total matter power spectrum from the Horizon set publicly available¹.

This manuscript is organized as follows. Section 2 describes the set of cosmological simulations used in this work. In section 3, we describe the method for computing the matter power spectra. Section 4 describes the baryonic correction model of Schneider & Teyssier (2015). We present our results in section 5, followed by a discussion and conclusions in sections 6 and 7, respectively. Unless otherwise noted, we adopt for this work a set of cosmological parameters consistent with *WMAP7* constraints (Komatsu et al. 2011) in accordance with the set-up of the hydrodynamical simulations, described in detail in the following section.

2 THE HORIZON SIMULATION SET

The Horizon set of simulations comprises three cosmological simulation boxes of $L = 100 h^{-1} \text{Mpc}$ on each side ran using the AMR code RAMSES (Teyssier 2002): Horizon-AGN (with full baryonic physics implementation), Horizon-noAGN (solely lacking AGN feedback in comparison to Horizon-AGN) and Horizon-DM (a DMO run). The three simulations share the same initial conditions and cosmological parameters. For this work, this is crucial, as we are particularly interested in the comparison between the three simulations. All of the runs adopt the cosmological parameters obtained by the Wilkinson Microwave Anisotropy Probe team (*WMAP7* cosmology, Komatsu et al. 2011): a total matter

¹ <https://www.horizon-simulation.org/catalogues.html>

density of $\Omega_m = 0.272$, a baryon density of $\Omega_b = 0.045$, a dark energy density of $\Omega_\Lambda = 0.728$, an amplitude of the matter power spectrum determined by $\sigma_8 = 0.81$, a Hubble constant of $H_0 = 70.4 \text{ km/s Mpc}^{-1}$, and the index of the primordial power spectrum given by $n_s = 0.967$.

There are 1024^3 dark matter (DM) particles in each box. The dark matter mass resolution is $M_{\text{DM, res}} = 8.3 \times 10^7 \text{ M}_\odot$ for the baryonic runs and $M_{\text{DM, res}} = 9.9 \times 10^7 \text{ M}_\odot$ for Horizon-DM. This difference in the mass of the DM particles between the DMO run and the baryonic run is due to keeping Ω_m constant between simulations.

Stellar particles form out of the gas distributed in the simulation grid. Star formation in each cell is modelled using a Schmidt law: $\dot{\rho}_* = \epsilon_* \rho / t_{\text{ff}}$, with $\dot{\rho}_*$ the star formation rate density in a simulation cell, ρ the gas density in the cell, $\epsilon_* = 0.02$ (Kennicutt 1998; Krumholz & Tan 2007) the constant star formation efficiency, and t_{ff} the local free-fall time of the gas. We allow star formation wherever the hydrogen gas number density exceeds $n_0 = 0.1 \text{ H cm}^{-3}$ according to a Poisson random process (Rasera & Teyssier 2006; Dubois & Teyssier 2008). The stellar mass resolution is $M_{*, \text{res}} = \rho_0 \Delta x^3 \simeq 2 \times 10^6 \text{ M}_\odot$. The AMR grid is refined following a quasi-Lagrangian criterion reaching up to 7 levels beyond the initial level, which allows us to reach a resolution of up to $\Delta x = 1 \text{ kpc}$. A new refinement stage is triggered if the number of DM particles in a cell is more than 8 or if the total baryonic mass in a cell is 8 times the initial DM mass resolution.

AGN feedback is incorporated in the Horizon-AGN simulation following the model presented in Dubois et al. (2012). We use a Bondi-Hoyle-Lyttleton accretion rate onto black hole particles, given by $\dot{M}_{\text{BH}} = 4\pi\alpha G^2 M_{\text{BH}}^2 \bar{\rho} / (\bar{c}_s^2 + \bar{u}^2)^{3/2}$, where M_{BH} is the black hole mass, $\bar{\rho}$ is the average gas density, \bar{c}_s is the average sound speed, \bar{u} is the average gas velocity relative to the black hole velocity, and α is a dimensionless boost factor. This boost factor is given by $\alpha = (\rho/\rho_0)^2$ when $\rho > \rho_0$ and $\alpha = 1$ otherwise (Booth & Schaye 2009), which allows us to account for our inability to capture the colder and higher density regions of the interstellar medium. The effective accretion rate onto black holes is not allowed to exceed the Eddington accretion rate: $\dot{M}_{\text{Edd}} = 4\pi GM_{\text{BH}} m_p / (\epsilon_r \sigma_T c)$, where σ_T is the Thompson cross-section, c is the speed of light, m_p is the proton mass, and ϵ_r is the radiative efficiency, assumed to be equal to $\epsilon_r = 0.1$ for the Shakura & Sunyaev (1973) accretion onto a Schwarzschild black hole. Two different modes of AGN feedback are implemented: the kinematic *radio* mode with 100% efficiency, operating when $\chi = \dot{M}_{\text{BH}} / \dot{M}_{\text{Edd}} < 0.01$, and the thermal *quasar* mode with 15% efficiency, active otherwise (see Dubois et al. 2014 for details). The Horizon-noAGN (Peirani et al. 2017) simulation lacks AGN feedback altogether, which allows us to isolate the impact of this mechanism on the total distribution of matter.

Gas cooling occurs by means of hydrogen and helium cooling down to a temperature of 10^4 K including the contribution from metals (Sutherland & Dopita 1993). Heating from a uniform UV background is implemented (Haardt & Madau 1996) after the reionization redshift, $z_{\text{reion}} = 10$. Metallicity is modeled as a passive variable of

the gas, and it changes according to the injection of gas ejecta from stellar winds and supernovae explosions. For modelling stellar feedback, we use a Salpeter (1955) initial mass function with a low-mass cut-off of 0.1 M_\odot and a high-mass cut-off of 100 M_\odot . The injection of mechanical energy from type II supernovae and stellar winds follows the STARBURST99 prescription (Leitherer et al. 1999, 2010), and the frequency of type Ia supernovae explosions adopted is from Gregg & Renzini (1983).

3 POWER SPECTRA COMPUTATION

The distribution of matter is quantified through its power spectrum, $P(k)$. If the density field in the simulation at a given redshift is given by $\rho(\mathbf{x}, z)$, we can characterize the inhomogeneities in this field via $\delta(\mathbf{x}, z) = \rho(\mathbf{x}, z) / \bar{\rho}(z) - 1$, where $\bar{\rho}(z)$ is the mean density of the universe at a certain redshift. The Fourier transform of $\delta(\mathbf{x}, z)$ is labelled $\tilde{\delta}(\mathbf{k}, z)$. The statistical properties of these inhomogeneities are described via the power spectrum,

$$\langle \tilde{\delta}(\mathbf{k}, z) \tilde{\delta}(\mathbf{k}', z) \rangle = (2\pi)^3 P(k) \delta_D^3(\mathbf{k} - \mathbf{k}'), \quad (1)$$

with δ_D^3 , the Dirac delta function. As the power spectrum has units of volume, we also work in terms of the dimensionless quantity Δ^2 , which is related to the power spectrum by

$$\Delta^2(k) \equiv \frac{k^3}{2\pi^2} P(k). \quad (2)$$

Nevertheless, we are most often interested in ratios between power spectra, which are insensitive to whether we are working with $P(k)$ or $\Delta^2(k)$.

The computation of the total matter power spectrum requires the mapping of each matter component onto a three-dimensional grid. In the case of DM, stars, and black holes, the mapping involves the application of a kernel to smoothly distribute the mass of each particle over neighbouring cells. In the case of the gas, the simulation outputs are given in terms of an AMR grid, with varying spatial resolution. To account for this, we convert the gas density field into a distribution of effective particles. This is done by looping over all cells in the AMR grid and placing a particle with the total mass of the cells in the centre-of-mass of the group. As a result, regions that are more refined will have a higher number of particles per unit volume. To determine the convergence of this method, we consider the case where we ignore the grid refinement above some cut-off scale. The result is that our fiducial method guarantees better than 1% convergence of the total matter power spectrum over our desired range of wavevectors when compared to the case when sub-structures are averaged at scales of $12 h^{-1} \text{ kpc}$ and above.

For each matter component (effective gas particles, DM particles, star and black hole particles) we map their mass to a uniform grid 1024 cells across a side using a piecewise quadratic spline (Hockney & Eastwood 1981). Each grid is Fourier transformed using the FOUR3M routine presented in Thacker & Couchman (2006), which is then convolved with a Green's function to minimize errors from the mass mapping (Hockney & Eastwood 1981), resulting in a Fourier grid for each component. Additionally, by summing these Fourier

grids we construct a total matter grid. The power spectrum of any individual matter component or of the total matter is then the mean of the squares of the corresponding grid values within fixed k bins. We have verified that adopting a 2048³ grid does not impact our results on the total matter power spectrum. For calculating cross correlations we first multiply the corresponding components' Fourier grids together, and then take the mean of the resulting grid values within fixed k bins.

The estimation of the auto-power spectra is affected by the discreteness of the tracers. In other words, there is an additive component to the power spectrum given by the contribution of “shot noise”,

$$P_{\text{shot}} = \frac{V}{N_{\text{eff}}}, \quad (3)$$

where V is the simulation volume. N_{eff} is the effective number of particles, which accounts for their difference in mass: $N_{\text{eff}} = (\sum_i^N m_i)^2 / (\sum_i^N m_i^2)$, and where N is the number of particles and m_i , their individual masses (Springel et al. 2017). In this analysis, we present total matter power spectra after subtracting the shot noise component. We have verified, however, that this subtraction does not modify our results given that we are usually restricted to scales where this component is usually sub-dominant.

Finally, the outputs of the different Horizon simulation runs that we compare in this work can differ slightly in the value of the scale factor. We account for these differences by performing a linear re-scaling based on the predicted linear growth function for our adopted cosmology, $D(z)$. In linear theory, the power spectrum at a given z can be obtained by re-scaling the $z = 0$ power spectrum: $P(k, z) = D^2(z)P(k, 0)$. There are limitations associated with this re-scaling, which can lead to residual differences in the matter power spectrum at large scales. For a detailed discussion of this effect, see Appendix A. Cosmic variance can also have an impact in our predictions, which is discussed in Section 5.4. Appendix B presents several convergence tests of our results.

4 BARYONIC CORRECTION MODEL

The BC model developed by Schneider & Teyssier (2015) was proposed to account for the impact of baryons on the total matter power spectrum by modifying the density field of dark-matter-only N -body simulations to mimic the effects of baryons from any underlying adopted feedback recipe. We summarise the BC model here and compare Horizon results to this model in the following section.

The main assumption behind the BC model is that haloes can be decomposed into four constituents: hot gas in hydrostatic equilibrium, ejected gas from feedback processes, stars from a central galaxy, and adiabatically relaxed dark matter. These four components alter the total distribution of matter, compared to that from dark matter-only simulations, by generating an excess at small scales due to efficient cooling of the gas leading to star formation, and a suppression at intermediate scales which depends on

the mass fraction of gas ejected by the AGN and its corresponding ejection radius. The components of the model are constrained by a combination of low resolution hydrodynamical simulations and observations. In particular, one wishes to have accurate models for the abundance fraction of each matter component, and its spatial profile. For example, Schneider & Teyssier (2015) adopt a parameterisation of the fraction of stars in a central galaxy proposed by Kravtsov et al. (2014), and a stellar profile following results from simulations of galaxy clusters by Mohammed et al. (2014).

Putting together the different model components, and studying the change in the predictions for a wide range of parameter space, Schneider & Teyssier (2015) suggested that an effective parameterisation of the impact of baryons on the total matter power spectrum would require capturing the *amount and scale of suppression* driven by gas ejection and the *enhancement of the small-scale power spectrum due to the stellar component*. As a consequence, the authors proposed a simplified parameterisation of baryonic effects on the matter power spectrum in the form of the product of two functions which represent these two effects:

$$F(k, z) \equiv \frac{P_{\text{BCM}}}{P_{\text{DMO}}} = G(k|M_c, \eta_b, z)S(k|k_s), \quad (4)$$

where P_{BCM} is the total matter power spectrum (“BCM” stands for the BC model) and P_{DMO} is the matter power spectrum for a dark-matter-only simulation with the same cosmology. G is a function that captures the effect of AGN on the distribution of matter, through the ejection of gas, and S represents the impact of star formation and baryonic cooling at small scales.

The suppression due to gas ejected by AGN is parameterized with the following function

$$G(k|M_c, \eta_b, z) = \frac{B(z)}{1 + [k/k_g(z)]^3} + [1 - B(z)], \quad (5)$$

where $B(z)$ parametrises the redshift dependence of the power suppression due to AGN feedback, with a characteristic redshift $z_c = 2.3$,

$$B(z) = B_0 \left[1 + \left(\frac{z}{z_c} \right)^{2.5} \right]^{-1}, \quad (6)$$

and an amplitude B_0 related to the mass of the galaxy clusters typically responsible for the suppression, M_c ,

$$B_0 = 0.105 \log_{10} \left(\frac{M_c}{M_\odot/h} \right) - 1.27. \quad (7)$$

The function $k_g(z)$ sets the typical scale of the gas ejection,

$$k_g(z) = \frac{0.7[1 - B(z)]^4 \eta_b^{-1.6}}{h/\text{Mpc}}, \quad (8)$$

parameterized by η_b , a parameter which relates the virial radius of the cluster to the distance at which the gas is ejected.

The stellar profile enhances the total matter power spectrum below scales of $k_s = 55 h \text{ Mpc}^{-1}$ with a quadratic polynomial

$$S(k|k_s) = 1 + (k/k_s)^2. \quad (9)$$

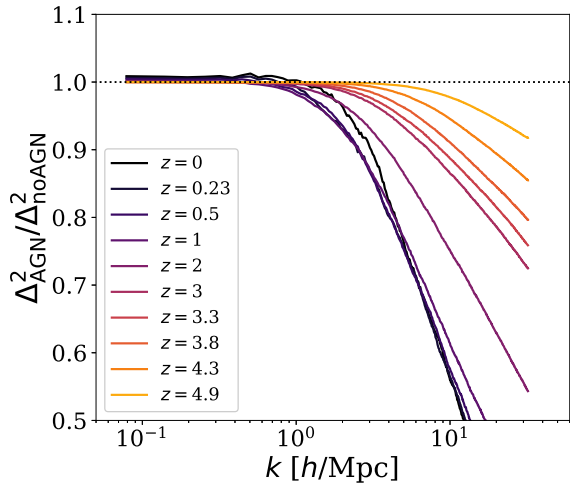


Figure 1. The impact of AGN feedback in the total matter power spectrum from the Horizon set across cosmic time, $0 \leq z < 6$. Darker colours correspond to lower redshifts. At intermediate scales ($k \sim 2 h/\text{Mpc}$), the AGN feedback suppression diminishes slightly from $z = 1$ to $z = 0$, an effect that we attribute to AGN feedback being insufficient to expel gas from the growing potential well of the most massive haloes.

The redshift dependence of the BC model has not been explored in detail. Schneider & Teyssier (2015) assumed that the model parameters were redshift independent in their original study, and discussed the predictions of the BC model in the range $z = 0 - 2$ under this assumption. By comparing the BC model to the Horizon predictions for the impact of baryons on the total matter power spectrum at different redshifts, we specifically test the validity of this assumption in the following sections.

5 RESULTS

5.1 The impact of AGN feedback

AGN feedback can have different consequences on the distribution of matter at small scales. It can heat the gas around a halo, preventing it from cooling, being accreted, and forming stars, or it can directly expel gas from a halo. We isolate the impact of AGN feedback on large-scale structures by comparing the total matter power spectrum of the Horizon-AGN and the Horizon-noAGN simulation runs.

Figure 1 shows the ratio between the total matter power spectrum in Horizon-AGN and Horizon-noAGN at several redshifts, in the range from $z = 4.9$ to $z = 0$. (For a discussion on the numerical convergence of our results, see appendix B.) As can be seen in Figure 1, AGN feedback suppresses power at small scales ($k \geq 10 h/\text{Mpc}$) as early as $z = 4.9$, and the magnitude of this suppression increases towards low redshift. At intermediate scales ($k \sim 2 h/\text{Mpc}$), the AGN feedback suppression diminishes slightly from $z = 1$ to $z = 0$.

Drawing on our previous analysis of the impact

of AGN feedback on the quenching of star formation (Beckmann et al. 2017), these results can be interpreted as follows. AGN feedback effectively regulates baryonic content at small scales, whether within smaller haloes or in the centre of larger ones, by heating the gas, redistributing it and preventing star formation. This process remains active throughout cosmic history. At redshifts $z \geq 1$, AGN in massive haloes drive large outflows and reduce inflows into their host galaxies, decreasing the power spectrum. In this redshift range, the suppression increases for any given k as the black holes powering AGN continue to grow. Around $z = 1$, several effects come into play that reduce the impact of AGN at a scale of a few h/Mpc . The biggest black holes accrete less efficiently, reducing their feedback energy (Volonteri et al. 2016). Effectively, AGN activity decreases as they enter into ‘‘maintenance’’ mode, and previously ejected gas can also be reaccreted by haloes as they continue to grow (McCarthy et al. 2011). As a result, gas is no longer ejected to large scales and previously ejected gas is reaccreted, so the suppression caused by AGN around $k \sim 2 h/\text{Mpc}$ decreases. The power spectrum remains suppressed at small scales as feedback continues to affect the centre of large haloes and the environment of smaller ones.

Figure 1 displays a large-scale excess of power below 1% for several redshifts. This is intriguing because given the same initial conditions, finite volume effects are expected to cancel at large scales. We have performed an extensive investigation of the source of this excess which we describe in detail in Appendix A. In brief, the simulation outputs we compare for the curves shown in Figure 1 differ slightly in their scale factor ($< 0.1\%$) and we have attempted to correct for the large-scale evolution of the power spectrum in the box by re-scaling it using the linear growth factor. However, even after this correction, our results are subject to 1% biases of the matter power spectrum. This is due to the box being too small to reach the linear regime at large scales and low redshift. These effects are sub-dominant compared to the impact of baryonic processes in which we are interested for this work.

5.2 The impact of baryons

In this section, we compare the total matter power spectra obtained from the baryonic simulation runs to that from the Horizon-DM run. Our results are shown in Figure 2 for Horizon-noAGN and Figure 3 for Horizon-AGN. The fractional impact of the effect of including baryons amply exceeds the 1% requirement on the knowledge of this observable at $k = 10 h/\text{Mpc}$ for future missions.

In Figure 2, we find that the impact of baryons on the total matter power spectrum at high redshift is to produce a suppression of power at scales above a few h/Mpc , accompanied by an enhancement at the smallest scales probed. This is not a consequence of AGN feedback, since this feedback mechanism is not present in Horizon-noAGN. The cause of the small scale enhancement is the additional cooling produced by the presence of baryons, which leads to an adiabatic contraction of the matter distribution at these scales (Blumenthal et al. 1986). Compared to Horizon-DM, the

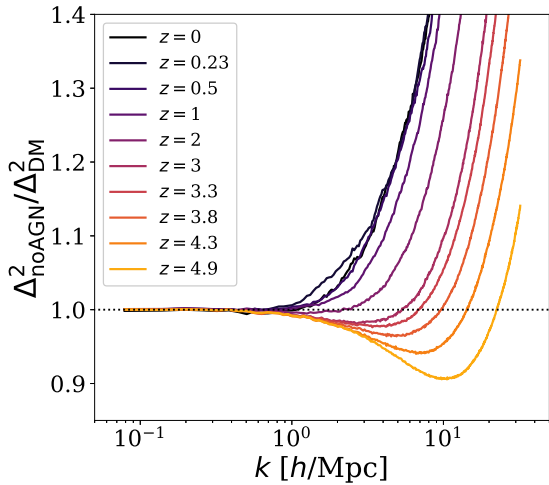


Figure 2. The fractional impact of baryons on the total matter power spectrum when comparing the Horizon-noAGN run (lacking AGN feedback) to the Horizon-DM run.

Horizon-noAGN run also shows a suppression of power of approximately 10% at scales of $k \simeq 10 h/\text{Mpc}$ at $z = 4.9$. This is a consequence of the delayed collapse of DM haloes given the pressure contributed by the presence of baryons. Feedback processes do not have an impact on results at this redshift, neither from AGN nor from supernovae. As redshift decreases, the suppression tends to be removed by the overall growth of structure.

Figure 3 shows the comparison between the Horizon-AGN run, including the impact of AGN feedback, and the Horizon-DM run, and is the main result of this work. The results at $z = 4.9$ are very similar to those shown in the previous figure. This is a consequence of the small impact of AGN feedback at this redshift, which was evidenced in Figure 1 in the previous sub-section.

The combined effect of the clustering of matter with the impact of AGN on its distribution leads to a non-monotonic redshift evolution of the ratios of power spectra between simulation runs. From $z = 4.9$ to $z = 3$, the effect of the AGN is not strong enough to compensate for adiabatic contraction. From $z = 3$ to $z = 1$, we find enhanced suppression due to the impact of AGN. From $z = 1$ to $z = 0$, the suppression is roughly constant but is shifted to smaller scales. As mentioned in the previous section, this behavior is a consequence of haloes becoming too massive for AGN feedback to efficiently eject (or prevent the accretion of) material. As a result, clustering increases at intermediate scales of $k \sim 2 h/\text{Mpc}$. In Section 5.4, we demonstrate that this specific behaviour is determined by the largest mass haloes formed in the simulation box.

5.3 Dark matter response to baryons

Do DMO simulations capture the dark matter component of the hydrodynamical simulations correctly? In other words,

do baryons significantly affect the distribution of dark matter? We answer this question in Figure 4, where we show the ratio between the dark matter power spectrum in Horizon-AGN and Horizon-DM in the range $0 < z < 2$. For comparison, we also show the ratio between Horizon-noAGN and Horizon-DM at $z = 0$ only. At $z = 2$, we find an excess of power at small scales, due to cooling of baryons, which enhances the gravitational potential wells of haloes in the hydrodynamical simulations and leads to adiabatic contraction of the DM component. There is also a decrement at intermediate scales, following the redistribution of gas. At lower redshift, the excess of power is transferred to smaller and smaller scales (haloes become more concentrated), while the impact of the ejected gas is to enhance the suppression at scales of $\sim 10 h/\text{Mpc}$ and compensate for this at scales of a few h/Mpc . As we discuss in Section 5.4, this specific scale-dependence is related to the limited cosmological volume of the simulation box, i.e., it is sensitive to cosmic variance. On the contrary, in the Horizon-noAGN simulation (black dashed curve), the net effect of baryonic processes is to produce an excess of power at small scales ($> 1 h/\text{Mpc}$).

5.4 Impact of cosmic variance

In Section 5.1, we asserted that the availability of baryonic and DMO runs with the same initial conditions allowed us to neglect finite volume effects at small wavenumber values. This does not guarantee, however, that we are free from the impact of cosmic variance in our results. We explore the consequences of the limited volume of the simulation box by dividing the Horizon boxes in 8 sub-volumes and obtaining predictions of the impact of baryons on the total matter power spectrum from these sub-volumes. The results are shown in the left panel of Figure 5, where the black thick solid line corresponds to the full volume results, and all other lines correspond to different sub-volumes, all at $z = 0$.

The dispersion of the gray curves gives us an estimation of the impact of cosmic variance on our results. In particular, we note that one of the sub-volumes displays an excess of power at $k \sim 3 h/\text{Mpc}$ in the total matter distribution with respect to the DM distribution in Horizon-DM. The comparison to the black solid curve suggests that our results from the full volume box are dominated by this particular sub-volume. The right panel of Figure 5 presents similar results for the power spectrum of the DM distribution alone. Most curves show some level of excess above zero at $k \sim 3 h/\text{Mpc}$, but the full volume results once more are dominated by one of the sub-volumes. The sub-volume with the largest excess at these scales is the only one to host haloes with masses above $10^{14.5} M_\odot$. These two haloes have masses of approximate $10^{14.8} M_\odot$ each. Intriguingly, the fact that the IllustrisTNG300 simulation, with a larger box size of 300 Mpc, also displays this pattern (Figure 9) suggests that this is robust to increasing the simulation volume. Overall, our results suggest that the accuracy of predictions for the impact of baryons on the matter power spectrum would improve by running larger volume hydrodynamic simulations with multiple realisations of the initial conditions.

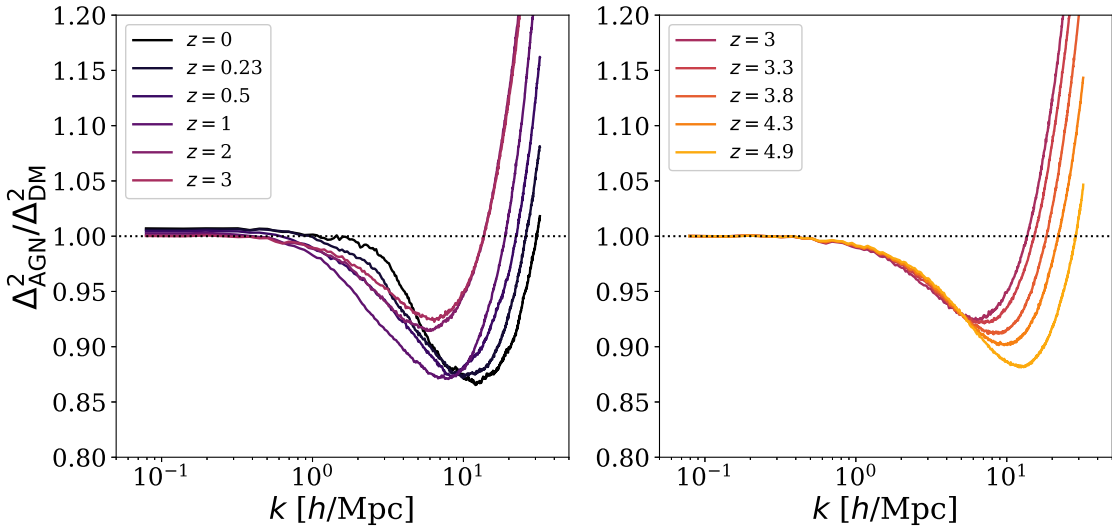


Figure 3. The fractional impact of baryons on the total matter power spectrum when comparing the Horizon-AGN run (with AGN feedback) to the Horizon-DM run. Results are split in two panels for different redshift ranges: $z \leq 3$ (left panel) and $z \geq 3$ (right panel).

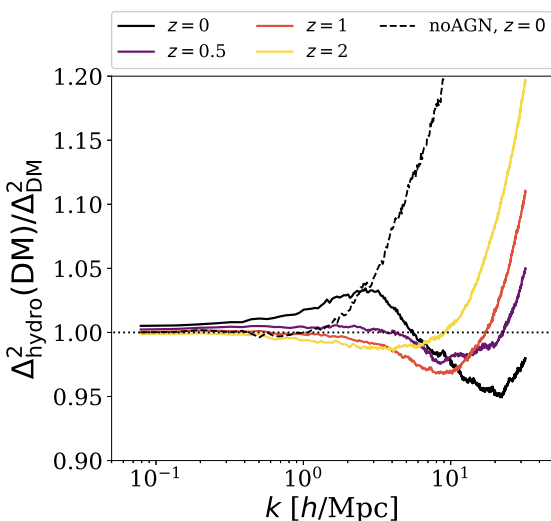


Figure 4. The fractional power spectrum of the *dark matter component* from the Horizon-AGN (solid) and the Horizon-noAGN (dashed) runs in the redshift range between $0 \leq z < 2$.

5.5 Comparison to other hydrodynamical simulations

Several other groups have quantified the impact of baryons on the matter power spectrum from their numerical simulations. Their simulations vary in the numerical technique implemented, volume, resolution and sub-grid recipes adopted for baryonic physics processes. In this section, we discuss how their results compare to Horizon-AGN. Figure 6 shows a comparison of the fractional impact of baryonic processes on the total matter power spectrum from dif-

ferent simulations at $z = 0$: the OverWhelmingly Large Simulations (van Daalen et al. 2011, we refer here to the ‘AGN’ run of OWLS which adopts a *WMAP7* cosmology), the EAGLE simulation (Hellwing et al. 2016), Illustris (Vogelsberger et al. 2014) and IllustrisTNG (Springel et al. 2017). The result from Horizon-noAGN is also shown for reference, in which case there is an enhancement of power due to efficient cooling of the gas, rather than a suppression of power.

While the qualitative behavior of all simulations is similar, with a suppression of power due to the effect of AGN feedback on the gas at $k \sim 10 h/\text{Mpc}$, the exact scale and strength of the suppression differs between them. Illustris shows the largest amount of suppression, reaching over 30% at scales of $k \sim 5 h/\text{Mpc}$. This simulation is calibrated to match the overall observed star formation history of the Universe, but despite this calibration, their radio mode of AGN feedback is known to be too aggressive, resulting in lower than observed gas fractions inside of massive haloes (Haider et al. 2016).

The OWLS ‘AGN’ run used by van Daalen et al. (2011) was calibrated to match the $M - \sigma$ relation (Booth & Schaye 2009; Schaye et al. 2010), similarly to Horizon-AGN, but differs in other sub-grid recipes (e.g., stellar initial mass function, stellar feedback prescription, black hole seeding, and thermal quasar AGN feedback for all accretion rates) and the numerical method implemented (smoothed-particle-hydrodynamics). McCarthy et al. (2010) have shown that this OWLS run reproduces the fraction of gas in massive haloes. However, those same authors suggested that the results on the properties of galaxy groups are sensitive to the choice of specific parameters which compensate for the over-cooling problem by increasing the minimum temperature that gas must reach by AGN feedback before releasing its

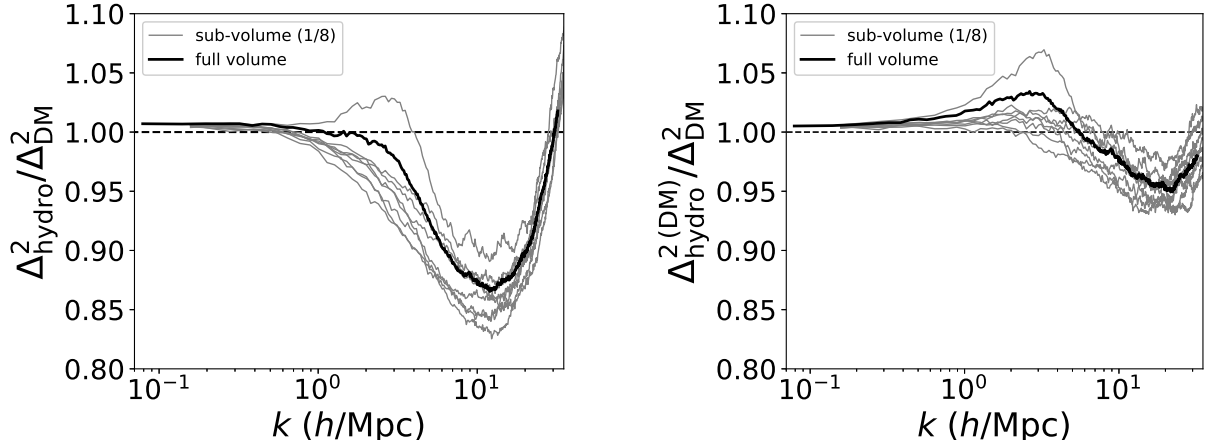


Figure 5. The impact of cosmic variance on the total matter power spectrum (left) and on the power spectrum of the dark matter component (right) at $z = 0$. The results for the full volume are shown in thick solid black; all other curves correspond to the 8 sub-volumes of the box. The large-scale excess is related to these scales becoming nonlinear at $z = 0$ (Appendix A). We have not applied any correction for shot noise in this figure, given that it is sub-dominant at this redshift.

energy (equivalent to a built-in gas density-dependent AGN duty cycle, Booth & Schaye 2009). At $z = 0$, OWLS predict significantly more suppression than Horizon-AGN, exceeding 20% at $k \sim 10 h/\text{Mpc}$. The impact of baryons in the case of OWLS is not as strong as in the Illustris simulation. This model has been widely used in the literature for cosmic shear data analysis (Mead et al. 2015), including recent cosmic shear survey results (Harnois-Déraps et al. 2015; Joudaki et al. 2017; Krause et al. 2017), and also for forecasting the performance of future surveys (Semboloni et al. 2011, 2013; Eifler et al. 2015).

The EAGLE simulation (Schaye et al. 2015) is a smoothed-particle-hydrodynamics simulation with similar volume to Horizon-AGN and full baryonic physics implementation. In this case, the simulation was calibrated to match the relation between stellar mass and halo mass, the present-day stellar mass function of galaxies and galaxy sizes. EAGLE predicts that the impact of baryons on the matter power spectrum is predominant at scales smaller than in Horizon-AGN, Illustris or OWLS. The difference in the preferred scale of suppression is particularly relevant to cosmic shear surveys adopting a cut on small scales in their analysis (Krause et al. 2017) instead of a marginalization strategy (Joudaki et al. 2017).

Springel et al. (2017) recently presented an analysis of the impact of baryons on the clustering of galaxies and matter in the IllustrisTNG simulations. IllustrisTNG is a set of cosmological simulation boxes with different volumes and physics implementations, and we are interested here in the comparison to the baryonic and DMO runs: “TNG100” and “TNG300”, which are 100 Mpc and 300 Mpc on each side, respectively. IllustrisTNG implements an updated AGN feedback recipe compared to the previous Illustris runs (Weinberger et al. 2017), among other changes (including SN feedback modelling). Their new AGN sub-grid model includes a different approach of radio kinetic feed-

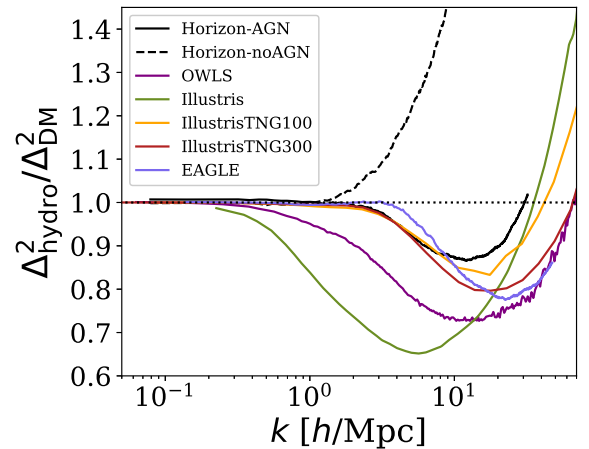


Figure 6. The impact of baryons on the total matter power spectrum ($\Delta^2_{\text{hydro}}/\Delta^2_{\text{DM}}$) in Horizon-AGN (solid black) and Horizon-noAGN (dashed black) compared to the results of other cosmological simulations at $z = 0$.

back mode compared to Illustris, which one is very similar to the one implemented in Horizon-AGN (Dubois et al. 2012) but with an isotropic momentum/energy injection (IllustrisTNG) instead of being jet-like shaped (Horizon-AGN). In Figure 6, we show the impact of baryons on the total matter power spectrum from IllustrisTNG100 and IllustrisTNG300 at $z = 0$ as obtained by Springel et al. (2017). The new IllustrisTNG runs show significantly lower impact of baryons on the distribution of matter, with a reduction of the overall amplitude of the effect and a restriction to smaller scales compared to Illustris. The IllustrisTNG300 results are similar to those obtained by EAGLE, despite different numeri-

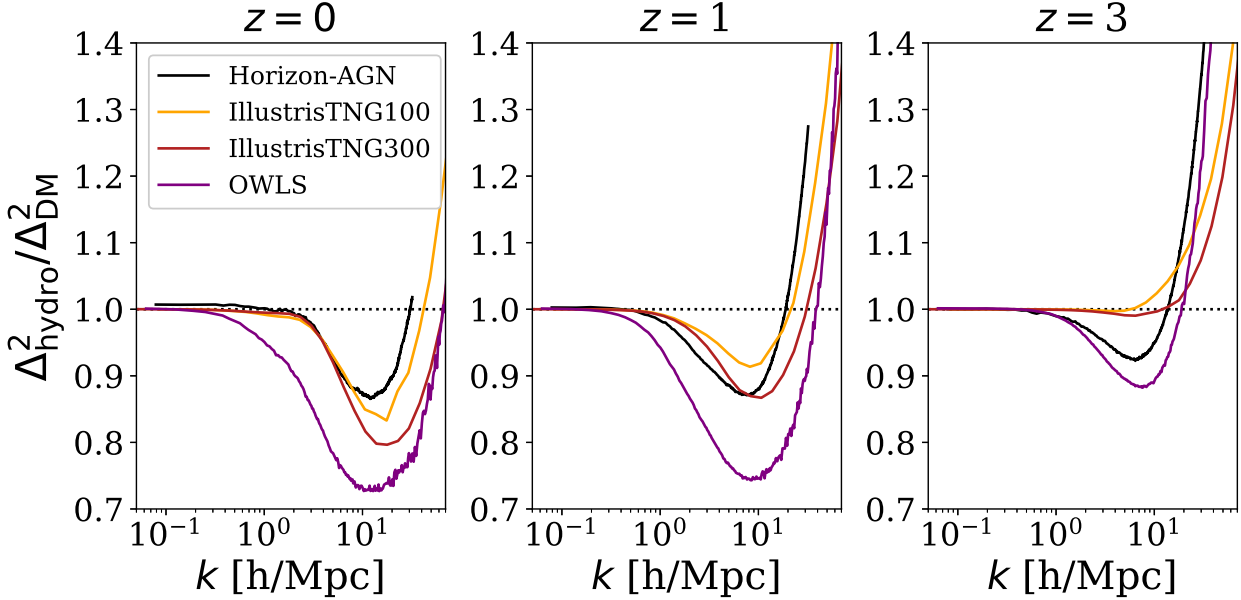


Figure 7. The impact of baryons on the power spectrum at redshifts $z = 0$ (left), $z = 1$ (middle) and $z = 3$ (right) for Horizon-AGN, OWLS and IllustrisTNG.

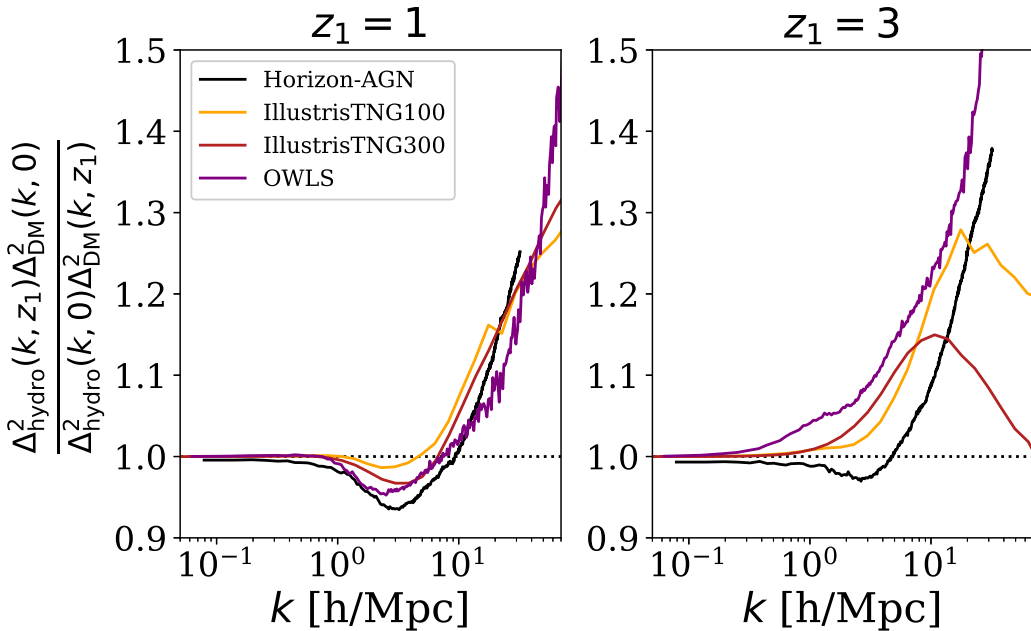


Figure 8. The impact of baryons on the power spectrum at a given $z = 0$ compared to $z_1 = 1, 3$. The y -axis can be interpreted as the ratio between effective scale-dependent growth functions: $\mathcal{D}^2(k, z) \equiv \Delta^2(k, z = 0) / \Delta^2(k, z_1)$. The left panel corresponds to the growth from $z_1 = 1$ to $z = 0$ and the right panel, from $z_1 = 3$ to $z = 0$. Both panels compare different curves for Horizon-AGN, OWLS and IllustrisTNG. The evolution of the impact of baryons is similar between the simulation in the range from $z_1 = 1$ to $z = 0$ but starts to differ at higher redshift.

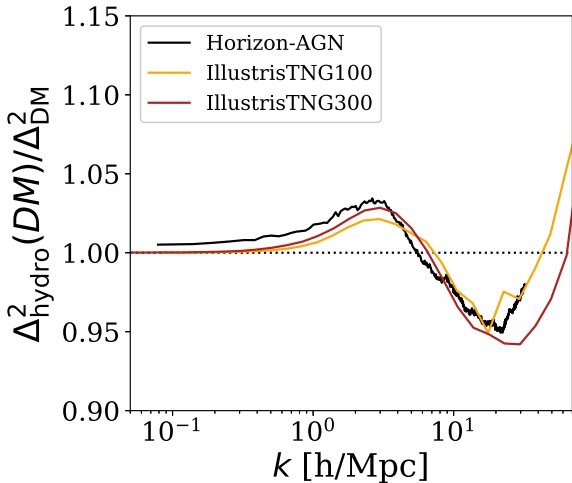


Figure 9. A comparison of the sensitivity of the DM component power spectrum to baryonic effects in IllustrisTNG (orange and red for TNG100 and TNG300, respectively) and in Horizon-AGN (black).

cal methods and sub-grid physics implementations. The discrepancy between IllustrisTNG100 and IllustrisTNG300 is attributed to differences in resolution and box size.

Compared to Horizon-AGN, IllustrisTNG simulations present enhanced suppression of the total matter power spectrum and a displacement of the peak of the suppression towards small scales at $z = 0$. Springel et al. (2017) and van Daalen et al. (2011) also presented results at higher redshifts for IllustrisTNG and OWLS, respectively, which allows us to compare the redshift evolution across these simulations in Figure 7. Compared to Horizon-AGN, the redshift evolution is much more dramatic in OWLS and IllustrisTNG from $z = 3$ to $z = 0$. The Horizon-AGN total matter power spectrum already shows signs of suppression at $z = 3$ due to AGN feedback (see discussion in Section 5.2), while IllustrisTNG only shows signs of gas cooling and adiabatic contraction at this redshift. IllustrisTNG undergoes a rapid redshift evolution towards $z = 0$, overtaking the suppression found in Horizon-AGN.

Figure 8 shows a slightly different rendering of the results presented in Figure 7. The two panels of Figure 8 show ratios of the impact of baryons between two redshifts: $z = 0$ and z_1 . The vertical axis represents an effective scale-dependent growth, defined as $\mathcal{D}^2(k, z_1) \equiv \Delta^2(k, z = 0)/\Delta^2(k, z_1)$. The panels compare $z = 0$ with $z_1 = 1$ (left), and $z = 0$ with $z_1 = 3$ (right). The predicted redshift evolution of the impact of baryons between these simulations from $z = 1$ to $z = 0$ is qualitatively similar. Discrepancies arise when comparing $z = 3$ and $z = 0$, in which case both OWLS and IllustrisTNG show stronger redshift evolution than Horizon. In the case of IllustrisTNG, the downturn of the curves at large k reflects a lack of suppression due to the presence of baryons at $z = 3$. Weak lensing surveys which aim to constrain the redshift evolution of the parameters of the equation of state of dark energy should accommodate

flexible models of the redshift evolution of this effect to avoid potential biases.

Finally, we have compared the impact of baryons in the DM distribution between Horizon-AGN and IllustrisTNG at $z = 0$ in Figure 9. Despite the differences evidenced for the suppression of the total matter power spectrum, the impact of baryonic effects on the DM distribution is similar across simulations. Although not shown here, the EAGLE team obtains similar results (Hellwing et al. 2016). All of the simulations feature enhanced clustering of the DM at very small scales (cuspier haloes due to adiabatic contraction), a suppression at intermediate scales and an enhancement at large scales. Nevertheless, Springel et al. (2017) has shown (their Figure 8) that the Illustris simulation produces a widely different prediction in this case, with a suppression at scales of a few h/Mpc . It is possible that the strong radio mode of AGN feedback used in Illustris is dominating the scales of the problem.

5.6 Effective modelling

In this section, we discuss the application of the BC model introduced in section 4 to our simulation results. In Schneider & Teyssier (2015), the BC model parameters were estimated from a combination of observational constraints and results from numerical simulations. These parameters are: M_c , which drives the amount of suppression in the power spectrum, η_b , the parameter that governs the scale of the suppression of power, and k_s , the wavenumber associated to the slope of the stellar density profile of the central galaxy. Figure 10 shows a comparison between the Horizon-AGN prediction of the fractional impact of baryons on the matter power spectrum (solid black curves) at $z = 0$ (left panel) and $z = 3$ (right panel) compared to the best fit BC model (in red).

The Horizon-AGN results are not well described by that fiducial choice of BC model parameters at $z = 0$. However, this should not come as a surprise since the BC model assumptions (such as the distribution of ejected gas or the stellar profiles) differ from the results of the Horizon-AGN run. We therefore find alternative best fit parameters that match our simulation results. The preferred parameters values are $M_c = 13.8 \text{ M}_\odot/h$, $k_s = 67 h/\text{Mpc}$ and $\eta_b = 0.17$ at this redshift. The lower value of η_b compared to the fiducial $\eta_b = 0.5$ value of Schneider & Teyssier (2015) indicates that the gas ejection of the Horizon-AGN run is less strong than the one assumed in the BC model. This is clearly shown in the comparison to the dashed and dotted-dashed curves, which show the impact of changing η_b to 0.3 and 0.5, respectively, while keeping M_c fixed to the best fit value. Our results also prefer a lower value of M_c compared to the fiducial $14.07 \text{ M}_\odot/h$ value adopted in Schneider & Teyssier (2015). This finding is related to the fractional content of gas in haloes, which is discussed in Section 6. The increase in k_s , on the other hand, compared to the fiducial $55 h/\text{Mpc}$ value corresponds to a higher concentration of matter at small scales.

The right panel of Figure 10 shows that the extrapolation of the $z = 0$ best fit case (in orange) predicts too little suppression of power at k of a few h/Mpc . This sug-

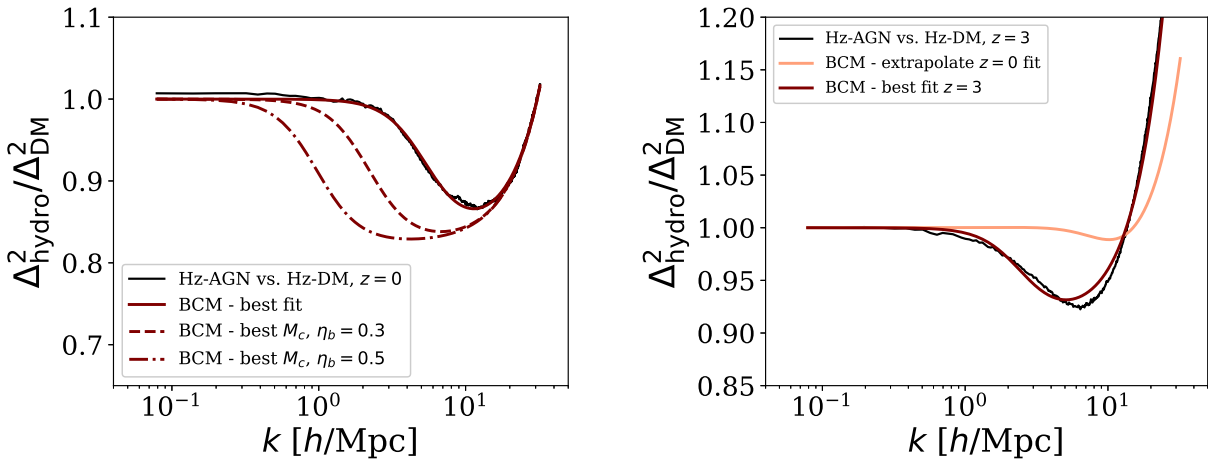


Figure 10. The impact of baryons on the total matter power spectrum ($\Delta_{\text{hydro}}^2/\Delta_{\text{DM}}^2$) in Horizon-AGN and a comparison to the BC model prediction at redshifts $z = 0$ (left panel) and $z = 3$ (right panel). The black curves show the Horizon-AGN results. The red curves correspond to the best fit BC model, freeing the parameters M_c , η_b and k_s at each redshift. The left panel also shows the impact of changing the η_b parameter to 0.3 (dashed) and 0.5 (dotted-dashed), values which are better motivated by observations, for comparison. The $z = 0$ fit is also extrapolated to $z = 3$ in the right panel and compared to the Horizon results (orange). The fiducial BC model redshift evolution together with the $z = 0$ best fit parameters does not match the BC model predictions.

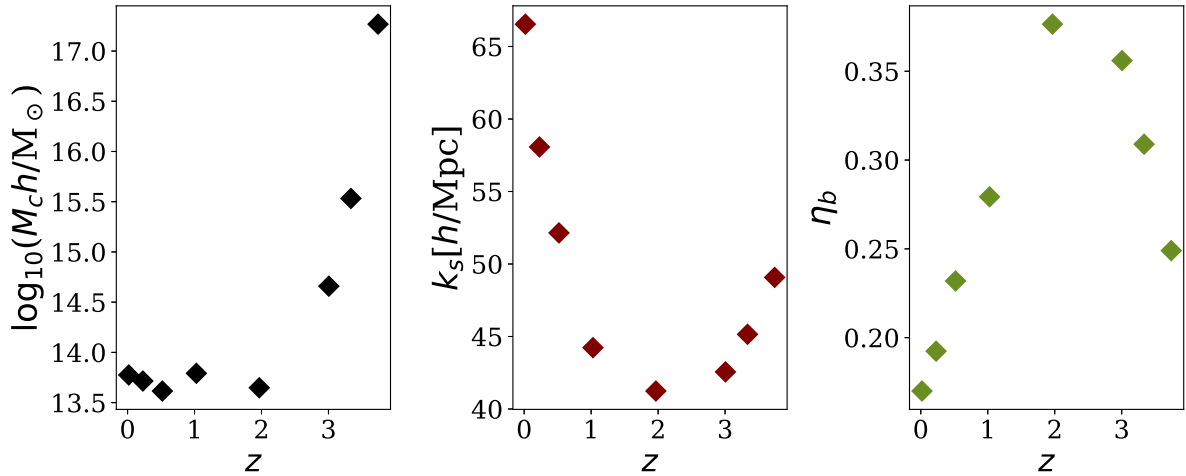


Figure 11. The best fit BC model parameters in each simulation snapshot in the range $0 < z < 4$. The left panel shows preferred values of M_c ; the middle panel, for k_s ; and the right panel, for η_b . The fiducial BC model assumption is to keep these parameters constant as a function of redshift.

gests that the BC model as formulated in Section 4 cannot describe the redshift evolution of the Horizon-AGN predictions. To account for a redshift evolution different than originally parameterized, we fit the BC model parameters to the simulation results at each redshift. The preferred parameter values are shown in Figure 11 as a function of redshift. We restrict to the redshift range $0 \leq z \leq 3.8$. This high redshift restriction is imposed due to the impact of resolution on the stellar population assembly of galaxies, which requires at least 1 Gyr to converge (Blaizot et al. 2004). We have verified that the majority of galaxies affected by AGN feedback

at $z = 3.8$, namely galaxies above a stellar mass threshold of $10^{9.5} \text{ M}_\odot$ (Beckmann et al. 2017), have stellar populations older than this threshold.

We find that the parameter M_c , which determines the amount of suppression in the total matter power spectrum and is related to the mass of the haloes responsible for it, is roughly constant in the range $0 < z < 2$, and it increases to higher redshift. The value of k_s , which represents the scale below which the contribution of the stellar profile sets in, decreases from $z = 4$ to $z = 3$, and then starts to increase again towards $z = 0$. Finally, η_b , which sets the physical scale

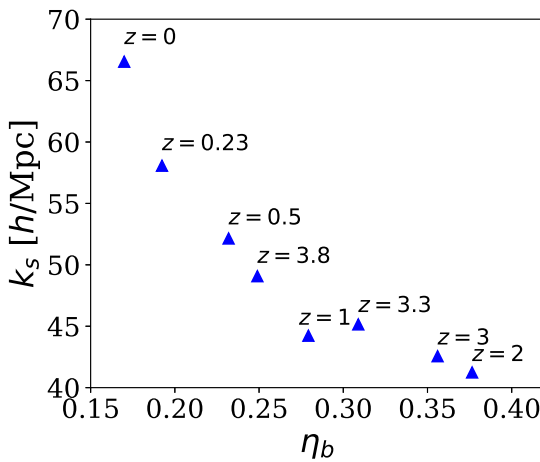


Figure 12. k_s and η_b preferred values for the BC model at each redshift (indicated by the label on each point). We find an anti-correlation between the two parameters.

for the suppression of power, also shows a non-monotonic evolution, with a peak at $z = 2$. The latter is a consequence of the redshift behaviour of the Horizon-AGN run discussed in Section 5.4 which is not captured by the BC model.

The values of these preferred parameters can be interpreted in the context of the BC model as follows. The typical mass of haloes where a large portion of the gas gets ejected by AGN processes is roughly constant between $0 \leq z < 2$. In Section 5.1, we drew similar conclusions based on our results from previous work (Beckmann et al. 2017). We suggested that, despite the availability of more massive haloes at low redshift, AGN feedback is not strong enough once in ‘‘maintenance’’ mode. At the same time, η_b decreases, restricting the impact of AGN on the total matter power spectrum to smaller and smaller scales and once again indicating a progressively waning impact of AGN on the total matter power spectrum. It is interesting to note that there is an anti-correlation between k_s and η_b as a result of the fits, shown in Figure 12. This is not built into the BC model, but can potentially suggest avenues for reducing its parameter space, as we discuss below.

Figure 11 also shows that the preferred value for M_c increases by several orders of magnitude between $z = 2$ and $z = 4$. This high redshift increase of M_c effectively reduces the number of haloes which can drive a suppression of power in the BC model. This is accompanied by a decrease of η_b in this redshift range, suggesting that gas ejection is less efficient than in the fiducial model considered in Schneider & Teyssier (2015), and the gas is expelled up to shorter distances from the center of haloes. A non-monotonic evolution of k_s , increasing from $z = 2$ to $z = 4$ is related to the effect of adiabatic cooling, which is already present as early as $z = 4.9$ in Figures 2 and 3.

The fiducial implementation of the BC model does not reproduce the redshift evolution of the Horizon total matter power spectra. We have found that an alternative with

i	A_i	B_i	C_i	D_i	E_i
2	80.6	0.86	-0.11	0.10	-2.05
1	-35.1	-1.29	0.67	-0.16	3.60
0	5.24	0.71	1.45	0.08	1.11

Table 1. Best fit parameters for $F(k, z)$ in the parameterisation proposed by Harnois-Déraps et al. (2015), as described by equation (11).

a small number of parameters which captures the Horizon results in the range $0 \leq z \leq 3.8$ is given by the following parameterisation of $F(k, z)$:

$$F(k, z) = \frac{1 + [k/\kappa_s(z)]^2}{1 + [k/\kappa_s(z)]^\beta}, \quad (10)$$

where $\kappa_s(z) = \kappa_{s,0} + \kappa_{s,1}z + \kappa_{s,2}z^2$ and $\kappa_{s,i}$ for $i = \{0, 1, 2\}$ are free parameters. The numerator of equation (10) captures the small scale enhancement in power due to adiabatic cooling, while the denominator models the suppression due to AGN feedback. The typical scale for both effects is connected to the value of $\kappa_s(z)$ as a consequence of the anti-correlation found between BC model parameters in Figure 12. The preferred values for the parameters are: $\beta = 1.39$, $\kappa_{s,0} = 28.5$, $\kappa_{s,1} = -11.9$ and $\kappa_{s,2} = 2.50$. For these parameters, $F(k, z)$ reproduces Horizon results within $< 5\%$ for all redshifts and scales considered. Physically driven modifications to the BC model to account for redshift evolution are not straightforward. This would require looking into the individual components of the model directly in the hydrodynamical simulation, which is the topic of our future work.

Other effective parameterisations of the impact of baryons on the matter power spectrum have been proposed in the literature. For example, in the work by Harnois-Déraps et al. (2015), an effective fitting function was proposed to model the impact of baryons on the total matter power spectrum from the OWLS simulations. The functional form proposed by Harnois-Déraps et al. (2015) was (b_m in their notation):

$$F(k, z) = 1 - A_z e^{(B_z x - C_z)^3} + D_z x e^{E_z x}, \quad (11)$$

where $x = \log_{10}(k/[h \text{ Mpc}^{-1}])$, the function A_z is parameterised as

$$A_z = A_2 a^2 + A_1 a + A_0, \quad (12)$$

with a the scale factor, and similarly for B_z , C_z , D_z and E_z . We find that this expression for $F(k, z)$ is sufficiently flexible to fit the Horizon results to within 3% across $z \leq 3.8$ with preferred parameters as listed in Table 1. The disadvantages of this approach are the large number of free parameters (15 in comparison to 3 in the fiducial BC model and 4 in equation 10) and the fact that there is no physical interpretation for them. Nevertheless, we make the parameters for this fitting function available here, as it might be useful for comparison to Harnois-Déraps et al. (2015).

Publicly available power spectra

The power spectra obtained from the Horizon set and used in this manuscript are made publicly available. These correspond to the redshifts labelled in Figure 1 up to $z = 3.8$, following the convergence criterion discussed above. Shot noise is subtracted.

To test the accuracy of the four-parameter fitting function $F(k, z)$ of equation (10), we obtained additional curves to those presented in Figure 3 at $z = 0.76$ and $z = 1.5$. We find that $F(k, z)$ reproduces those results within 3.4% and 4.3%, respectively. On the other hand, directly interpolating the set of public power spectra with a cubic spline results in uncertainties of up to 1.5% and 2.2% for the fractional impact of baryons on the total matter power spectrum at $z = 0.76$ and $z = 1.5$, respectively. The individual power spectra (with and without baryons) are interpolated with much larger uncertainty ($\sim 8\%$) than their ratio.

6 DISCUSSION

The results presented in this work suggest that there is significant dispersion between predictions of the impact of baryons on the total matter power spectrum from different cosmological hydrodynamical simulations (Figure 6) at $z = 0$. EAGLE shows the smallest impact from baryons on the distribution of matter at $k < 10 h/\text{Mpc}$, while the original Illustris run is most impacted. In addition, simulations also predict different redshift evolution of this effect. Distinguishing between these different scenarios is impossible from simulation data.

Observational constraints can be used to distinguish between different predictions. Numerous observations are already available that test the accuracy of the hydrodynamical simulations across the redshift range of future surveys. Those observations include galaxy luminosity and mass functions (see a comparison of Horizon-AGN results to these observations in Kaviraj et al. 2017) or stellar to halo mass relations (Leauthaud et al. 2012; Wojtak & Mamon 2013; Velander et al. 2014; Han et al. 2015; van Uitert et al. 2016), for example.

In their work, Schneider & Teyssier (2015) used constraints on the fraction of bound gas within haloes to inform the BC model. Similarly, one can compare how well the simulations reproduce this specific observation, as we show in Figure 13. For each halo in Horizon-AGN we have extracted the fraction of the mass in gas within the volume enclosing a sphere of 500 times the critical density of the Universe, and we show it as a function of M_{500} , the total mass of the halo within the corresponding radius (r_{500}). Figure 13 shows that the Horizon-AGN simulation overpredicts the fraction of gas in massive haloes (black points) with respect to the parametrised observational results at $z = 0$ described by the black solid line (Schneider & Teyssier 2015). This is the cause for our lower preferred value of M_c in the BC model fits of Section 5.6, shown in Figure 10. The excess gas fraction in haloes suggests a lower strength of AGN feedback, which in the BC model is associated with a lower halo mass.

The shaded areas in Figure 13 show the fraction of

gas at $z = 0$ in the haloes of the cosmo-OWLS simulations (Le Brun et al. 2014). The gray area corresponds to the AGN8.0 model, which shares the same parameters as the OWLS ‘AGN’ run. The orange area corresponds to the AGN8.5 cosmo-OWLS model, which adopts a slightly increased heating temperature for AGN feedback (Booth & Schaye 2009). Using synthetic X-ray observations to estimate the halo mass and gas mass fraction of simulated clusters, Le Brun et al. (2014) found that, in a *WMAP7* cosmology, observational results lie in between the predictions of the cosmo-OWLS AGN8.0 and AGN8.5 runs. The red crosses and green triangles in Figure 13 represent Horizon-AGN results at $z = 1$ and $z = 2$, respectively. The fraction of gas inside haloes decreases towards $z = 0$.

We emphasise that while some mitigation strategies for the impact of baryons on the matter power spectrum and cosmological observables from galaxy surveys have been proposed (Semboloni et al. 2011, 2013; Harnois-Déraps et al. 2015; Mead et al. 2015), these have often relied on the OWLS predictions from van Daalen et al. (2011) alone, the first predictions on the impact of baryons on the total matter power spectrum to become publicly available. Eifler et al. (2015) is the exception, using the OWLS results in combination with two other sets of simulations. It is known that the success of these mitigation techniques depends on the ability to cover the parameter space of possible models (Mohammed & Gnedin 2017). Our results suggest that hydrodynamical simulations can give very different predictions for the amplitude-, redshift- and scale-dependence of the effect. In principle, the success of the available mitigation strategies should be tested against the different cosmological simulations.

Semboloni et al. (2011) pointed out potential degeneracies between the impact of baryons on the total matter power spectrum and other physical processes. These included estimates of neutrino mass, the running of the spectral index to constrain inflation and the nature of dark matter. In this regard, Villaescusa-Navarro et al. (2017) recently suggested that the impact of neutrinos can be isolated from that of baryonic processes because of the distinct scale- and redshift-dependence of the effects. On the other hand, other degeneracies remain unexplored, including degeneracies with other astrophysical and observational systematics that affect weak lensing (photometric redshifts, source blending, intrinsic galaxy alignments). In particular, Hearin et al. (2012) showed that increased uncertainties in photometric redshifts can make requirements on knowledge of the power spectrum more stringent.

Finally, considering that the statistical uncertainties on the total matter power spectrum from future weak lensing surveys (percent level) will be much smaller than the effect of baryons on this observable, it is expected that weak lensing measurements in the next decade will be able to distinguish between different AGN feedback models (Foreman et al. 2016), although this depends on the level of control over weak lensing systematics at small scales.

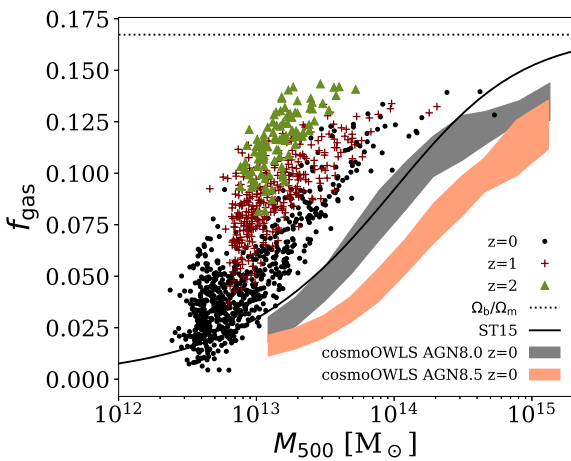


Figure 13. The fraction of gas by mass in haloes, f_{gas} , as a function of the mass enclosed within r_{500} . The dotted line represents the baryon fraction for our adopted cosmology. The solid line is a parameterisation of $z = 0$ observational constraints presented in Schneider & Teyssier (2015). The black, red and green dots correspond to Horizon-AGN results at redshifts $z = 0$, $z = 1$ and $z = 2$, respectively. The shaded area indicate results from the cosmo-OWLS simulations (Le Brun et al. 2014), specifically: the gray area corresponds to the AGN8.0 model (similar to the one adopted in the OWLS AGN run) and the orange area, to the AGN8.5 model, with increased heating temperature in the AGN feedback implementation.

7 CONCLUSIONS

In this work, we presented results on the distribution of matter at cosmological scales from the Horizon set of simulations in terms of the total matter power spectrum between $z = 0$ and $z = 5$. We found that intermediate scales ($1 < k < 10 h/\text{Mpc}$) are suppressed by 5–15% with respect to the DMO run. At smaller scales, the power spectrum is enhanced due to efficient cooling and star formation. The Horizon-noAGN simulation also displays suppression at high redshift compared to the DMO run, associated to the additional pressure provided by the baryons. At low redshifts, Horizon-noAGN is purely enhanced with respect to the DMO run. We have also quantified the impact of baryons on the distribution of dark matter in the simulation, finding it to be of a few percent at low redshift. The results are subject to cosmic variance and the presence of massive haloes, which we have verified by splitting the simulation volume into 8 sub-volumes.

A comparison between the Horizon set and other cosmological hydrodynamics simulations (Section 5.5) shows that the impact of baryons is smaller in Horizon, of typically $\sim 12\%$ at a scale of $k \sim 10 h/\text{Mpc}$ at $z = 0$. Nevertheless, the fraction of gas inside haloes in the Horizon-AGN simulation is enhanced compared to low redshift observations, suggesting AGN feedback is not strong enough to eject or prevent the infall of material into haloes (Figure 13). In this

regard, the cosmo-OWLS AGN8.0 and AGN8.5 runs are in better agreement with observations.

The redshift evolution is also different between simulations, with Horizon displaying a non-monotonic trend associated with the impact of gas pressure and AGN feedback, which competes with the growth of structure between $0 < z < 6$. The Horizon results are well-approximated by the BC model of Schneider & Teyssier (2015) at $z = 0$, but with different preferred values for the parameters that determine the amount and scale of suppression of power due to baryons, and a smaller typical scale for the stellar component. The redshift dependence of our results also differs from the BC model prediction and we have provided an effective parameterisation with 4 free parameters which approximates the Horizon results within $< 5\%$ at all redshifts. In the future, we plan to carry out a more detailed comparison between the BC model assumptions and components and the simulation predictions.

The total matter power spectra obtained in this work from Horizon-AGN, Horizon-noAGN and Horizon-DM have been made publicly available.

ACKNOWLEDGMENTS

This work has made use of the HPC resources of CINES (Jade and Occigen supercomputer) under the time allocations 2013047012, 2014047012 and 2015047012 made by GENCI. This work is partially supported by the Spin(e) grants ANR-13-BS05-0005 (<http://cosmicorigin.org>) of the French Agence Nationale de la Recherche and by the ILP LABEX (under reference ANR-10-LABX-63 and ANR-11-IDEX-0004-02). We thank S. Rouberol for running smoothly the Horizon cluster for us. Part of the analysis of the simulation was performed on the DiRAC facility jointly funded by STFC, BIS and the University of Oxford.

NEC acknowledges support from a Beecroft Postdoctoral Research Fellowship and a Royal Astronomical Society Research Fellowship. RSB acknowledges support from STFC. AMCLB was supported by the European Research Council under the European Union’s Seventh Framework Programme (FP7/2007-2013) / ERC grant agreement number 340519.

We are grateful to Volker Springel, Ruediger Pakmor, Mark Vogelsberger, Lars Hernquist and Wotjek Hellwing for providing the matter power spectra from IllustrisTNG, Illustris and EAGLE for comparison to Horizon-AGN in this work. We thank the OWLS team for making their results publicly available. We are grateful to Joachim Harnois-Déraps for useful discussions and to Robert J. Thacker for help setting up and running `pispec4` for the power spectrum computation. Some of the theoretical predictions used in this work have made use of the Core Cosmology Library², which also uses the CLASS software (Blas et al. 2011).

² <https://github.com/LSSTDESC/CCL>

References

Bartelmann M., Schneider P., 2001, *Phys. Rep.*, 340, 291

Beckmann R. S., et al., 2017, *MNRAS*, 472, 949

Blaizot J., Guiderdoni B., Devriendt J. E. G., Bouchet F. R., Hatton S. J., Stoehr F., 2004, *MNRAS*, 352, 571

Blas D., Lesgourges J., Tram T., 2011, *JCAP*, 7, 034

Blumenthal G. R., Faber S. M., Flores R., Primack J. R., 1986, *ApJ*, 301, 27

Booth C. M., Schaye J., 2009, *MNRAS*, 398, 53

Dubois Y., Teyssier R., 2008, *A&A*, 477, 79

Dubois Y., Devriendt J., Slyz A., Teyssier R., 2012, *MNRAS*, 420, 2662

Dubois Y., et al., 2014, *MNRAS*, 444, 1453

Dubois Y., Peirani S., Pichon C., Devriendt J., Gavazzi R., Welker C., Volonteri M., 2016, *MNRAS*, 463, 3948

Eifler T., Krause E., Dodelson S., Zentner A. R., Hearn A. P., Gnedin N. Y., 2015, *MNRAS*, 454, 2451

Fedeli C., 2014, *JCAP*, 4, 028

Foreman S., Becker M. R., Wechsler R. H., 2016, *MNRAS*, 463, 3326

Green J., et al., 2011, preprint, ([arXiv:1108.1374](https://arxiv.org/abs/1108.1374))

Greggio L., Renzini A., 1983, *A&A*, 118, 217

Haardt F., Madau P., 1996, *ApJ*, 461, 20

Haider M., Steinhauser D., Vogelsberger M., Genel S., Springel V., Torrey P., Hernquist L., 2016, *MNRAS*, 457, 3024

Han J., et al., 2015, *MNRAS*, 446, 1356

Harnois-Déraps J., van Waerbeke L., Viola M., Heymans C., 2015, *MNRAS*, 450, 1212

Hearin A. P., Zentner A. R., Ma Z., 2012, *JCAP*, 4, 034

Heitmann K., Lawrence E., Kwan J., Habib S., Higdon D., 2014, *ApJ*, 780, 111

Hellwing W. A., Schaller M., Frenk C. S., Theuns T., Schaye J., Bower R. G., Crain R. A., 2016, *MNRAS*, 461, L11

Heymans C., et al., 2012, *MNRAS*, 427, 146

Hockney R. W., Eastwood J. W., 1981, Computer Simulation Using Particles. McGraw-Hill

Howlett C., Lewis A., Hall A., Challinor A., 2012, *JCAP*, 4, 27

Huff E. M., Hirata C. M., Mandelbaum R., Schlegel D., Seljak U., Lupton R. H., 2014, *MNRAS*, 440, 1296

Huterer D., Takada M., 2005, Astroparticle Physics, 23, 369

Ivezic Z., et al., 2008, preprint, ([arXiv:0805.2366](https://arxiv.org/abs/0805.2366))

Joudaki S., et al., 2017, *MNRAS*, 471, 1259

Kaviraj S., et al., 2017, *MNRAS*, 467, 4739

Kennicutt Jr. R. C., 1998, *ApJ*, 498, 541

Kilbinger M., 2015, Reports on Progress in Physics, 78, 086901

Kitching T. D., Verde L., Heavens A. F., Jimenez R., 2016, *MNRAS*, 459, 971

Komatsu E., Smith K. M., Dunkley J., et al. 2011, *ApJ Sup.*, 192, 18

Krause E., et al., 2017, preprint, ([arXiv:1706.09359](https://arxiv.org/abs/1706.09359))

Kravtsov A., Vikhlinin A., Meshcheryakov A., 2014, preprint, ([arXiv:1401.7329](https://arxiv.org/abs/1401.7329))

Krumholz M. R., Tan J. C., 2007, *ApJ*, 654, 304

Laureijs R., 2009, preprint, ([arXiv:0912.0914](https://arxiv.org/abs/0912.0914))

Laureijs R., et al., 2011, preprint, ([arXiv:1110.3193](https://arxiv.org/abs/1110.3193))

Le Brun A. M. C., McCarthy I. G., Schaye J., Ponman T. J., 2014, *MNRAS*, 441, 1270

Le Brun A. M. C., McCarthy I. G., Schaye J., Ponman T. J., 2017, *MNRAS*, 466, 4442

Leauthaud A., et al., 2012, *ApJ*, 744, 159

Leitherer C., Schaerer D., Goldader J. D., et al. 1999, *ApJ Sup.*, 123, 3

Leitherer C., Ortiz Otálvaro P. A., Bresolin F., Kudritzki R.-P., Lo Faro B., Pauldrach A. W. A., Pettini M., Rix S. A., 2010, *ApJ Sup.*, 189, 309

McCarthy I. G., et al., 2010, *MNRAS*, 406, 822

McCarthy I. G., Schaye J., Bower R. G., Ponman T. J., Booth C. M., Dalla Vecchia C., Springel V., 2011, *MNRAS*, 412, 1965

Mead A. J., Peacock J. A., Heymans C., Joudaki S., Heavens A. F., 2015, *MNRAS*, 454, 1958

Mohammed I., Gnedin N. Y., 2017, preprint, ([arXiv:1707.02332](https://arxiv.org/abs/1707.02332))

Mohammed I., Seljak U., 2014, *MNRAS*, 445, 3382

Mohammed I., Martizzi D., Teyssier R., Amara A., 2014, preprint, ([arXiv:1410.6826](https://arxiv.org/abs/1410.6826))

Peirani S., et al., 2017, *MNRAS*, 472, 2153

Rasera Y., Teyssier R., 2006, *A&A*, 445, 1

Salpeter E. E., 1955, *ApJ*, 121, 161

Schaye J., et al., 2010, *MNRAS*, 402, 1536

Schaye J., et al., 2015, *MNRAS*, 446, 521

Schneider A., Teyssier R., 2015, *JCAP*, 12, 049

Schneider A., et al., 2016, *JCAP*, 4, 047

Seljak U., 2000, *MNRAS*, 318, 203

Semboloni E., Hoekstra H., Schaye J., van Daalen M. P., McCarthy I. G., 2011, *MNRAS*, 417, 2020

Semboloni E., Hoekstra H., Schaye J., 2013, *MNRAS*, 434, 148

Shakura N. I., Sunyaev R. A., 1973, *A&A*, 24, 337

Springel V., et al., 2017, preprint, ([arXiv:1707.03397](https://arxiv.org/abs/1707.03397))

Sutherland R. S., Dopita M. A., 1993, *ApJ Sup.*, 88, 253

Takahashi R., Sato M., Nishimichi T., Taruya A., Oguri M., 2012, *ApJ*, 761, 152

Tenneti A., Mandelbaum R., Di Matteo T., Feng Y., Khandai N., 2014, *MNRAS*, 441, 470

Teyssier R., 2002, *A&A*, 385, 337

Thacker R. J., Couchman H. M. P., 2006, *Computer Physics Communications*, 174, 540

Troxel M. A., et al., 2017, preprint, ([arXiv:1708.01538](https://arxiv.org/abs/1708.01538))

Tyson J. A., Valdes F., Wenk R. A., 1990, *ApJ Let.*, 349, L1

Velander M., et al., 2014, *MNRAS*, 437, 2111

Villaescusa-Navarro F., Banerjee A., Dalal N., Castorina E., Scoccimarro R., Angulo R., Spergel D. N., 2017, preprint, ([arXiv:1708.01154](https://arxiv.org/abs/1708.01154))

Vogelsberger M., et al., 2014, *Nature*, 509, 177

Volonteri M., Dubois Y., Pichon C., Devriendt J., 2016, preprint, ([arXiv:1602.01941](https://arxiv.org/abs/1602.01941))

Weinberg D. H., Mortonson M. J., Eisenstein D. J., Hirata C., Riess A. G., Rozo E., 2013, *Phys. Rep.*, 530, 87

Weinberger R., et al., 2017, *MNRAS*, 465, 3291

Wittman D. M., et al., 2002, in Tyson J. A., Wolff S., eds, *Proc. SPIE* Vol. 4836, Survey and Other

Telescope Technologies and Discoveries. pp 73–82
 (arXiv:astro-ph/0210118), doi:10.1111/12.457348

Wojtak R., Mamon G. A., 2013, *MNRAS*, 428, 2407

de Jong J. T. A., et al., 2013, *The Messenger*, 154, 44

van Daalen M. P., Schaye J., Booth C. M., Dalla Vecchia C., 2011, *MNRAS*, 415, 3649

van Uitert E., et al., 2016, *MNRAS*, 459, 3251

APPENDIX A: ACCURACY AT LARGE SCALES

Several of the results presented in this manuscript (Figs. 1 through 10) refer to ratios between power spectra of Horizon-AGN, Horizon-noAGN and Horizon-DM, the three simulations of the Horizon set. In taking these ratios, it is often the case that the redshifts being compared across runs differ slightly. For example, one of the snapshots is extracted at redshift z_1 , while the other one is extracted at $z_1 + \delta z$. To first order, we can and we do correct for this effect by re-scaling the power spectra using the linear growth function. In other words, in presenting the ratio of power spectra from simulations A (at z_1) and B (at $z_1 + \delta z$), we estimate

$$\frac{\Delta_A^2(z_1)}{\Delta_B^2(z_1)} = \frac{D^2(z_1 + \delta z)}{D^2(z_1)} \frac{\Delta_A^2(z_1)}{\Delta_B^2(z_1 + \delta z)}, \quad (\text{A1})$$

where D is the linear growth factor normalized to 1 at $z = 0$. Even after performing this correction, we have found residual effects that affect the ratio of power spectra across simulations at large scales at the 1% level, which can be clearly seen in Figures 1 and 3 at $z = 0$ for example.

This effect arises because the re-scaling procedure based on the linear growth function is insufficient to remove the large-scale excess power. We have verified that this is the case by performing the following comparison. For each of the simulation runs, we compared power spectra at two different redshifts by taking their ratio at large-scales normalized by the growth factor such that

$$\chi \equiv \frac{D^2(z_2)}{D^2(z_1)} \frac{\Delta_A^2(z_1)}{\Delta_A^2(z_2)}. \quad (\text{A2})$$

In practice, we chose z_1 and z_2 to be consecutive snapshots among those presented in Figure 1. The comparison demonstrated that indeed equation (A2) deviates from unity by $\sim 1\%$ at large scales. Based on the results of Schneider et al. (2016), who studied the convergence of the large-scale power in N -body simulations with different box sizes, this result is expected. Schneider et al. (2016) indeed suggest that a minimum volume of $(500 h/\text{Mpc})^3$ is required for the simulation to probe linear scales at $z = 0$.

We also considered the possibility of a transfer of power from small to large-scales due to the refinement scheme of the RAMSES code. We ruled out this hypothesis by comparing the matter power spectrum from the Horizon-DM simulation at $z = 2$ to that of an additional unrefined run with 1024^3 particles extracted at the same redshift. We show this comparison in the orange curve of Figure A1, which demonstrates that any large-scale difference in power is much less than 1% in this case.

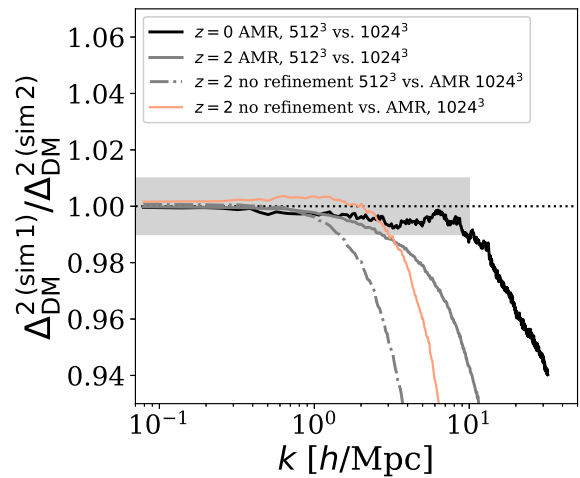


Figure A1. The impact of resolution (i.e., number of particles) in the matter power spectrum of the DMO run. The figure shows the ratio between the power spectrum from different low resolution runs and our fiducial run with 1024^3 particles. The black curve shows the results for the run with 512^3 particles and refinement at $z = 0$; the gray curve corresponds to the same simulation at $z = 2$. The dot-dashed curve corresponds to the $z = 2$ case without AMR. The orange curve corresponds to an unrefined run with 1024^3 particles at $z = 2$. The shaded area represents $\pm 1\%$ accuracy.

APPENDIX B: CONVERGENCE TESTS

In this section, we study the convergence properties of the matter power spectrum at small scales in the Horizon simulation. The fiducial resolution of Horizon is 1024^3 particles, with an approximate dark matter mass of $8 \times 10^7 M_\odot$ in the baryonic runs, and slightly higher in the DMO run to accommodate the same Ω_m value. To estimate the convergence rate of the simulation, we run two other DMO boxes with 512^3 particles (with and without refinement) and a 1024^3 box without refinement, and we compare the matter power spectrum estimated from those boxes to the fiducial one in this work at $z = 2$ and $z = 0$.

The results are shown in Figure A1. The shaded area in the figure represents the target of 1% accuracy below $k < 10 h/\text{Mpc}$. The results for $z = 2$ (solid gray) indicate that, due to resolution effects on the number of particles, this accuracy is achieved at $k < 3 h/\text{Mpc}$. The additional impact of the refinement of the grid is then evidenced in the comparison between the solid gray curve and the dotted-dashed gray curve, which corresponds to the unrefined 512^3 simulation at $z = 2$. The reduction in the convergence scale defined by the 1% accuracy requirement is of a factor of ~ 2 for the dotted-dashed gray curve. Focusing now on the orange curve which indicates the results of the 1024^3 unrefined run at $z = 2$, we find that 1% accuracy is achieved at $k = 3 h/\text{Mpc}$. Extrapolating from the 512^3 case, this suggests that the 1024^3 refined simulation should have achieved 1% convergence at $k \sim 6 h/\text{Mpc}$ at least. Its convergence rate compared to a hypothetically 2048^3 refined simulation should be shallower

than in the case of the orange curve, thus suggesting we very likely achieve a few percent convergence throughout all the scales of interest in this work.

At $z = 0$, the convergence rate is much better than at $z = 2$. This is evidenced from the results of the black solid curve, which shows the comparison of the 512^3 refined simulation to the 1024^3 refined simulation at $z = 0$. In this case, the convergence scale is extended to $k \sim 10 h/\text{Mpc}$, thus allowing us to infer that the 1024^3 runs have converged to approximately twice that value. Note that the convergence rate in the case of the presence of baryons should be even better due to the increased number of particles (roughly a factor of 2 at $z = 0$).

Our results are in good agreement with Schneider et al. (2016), who studied the accuracy of matter power spectrum predictions from DMO simulations with a variety of box sizes and resolutions. Their results suggested that per cent accuracy can be achieved up to $k \sim 4 h/\text{Mpc}$ for a $(512 \text{ Mpc}/h)^3$ simulation with 1024^3 particles. Re-scaling the wavenumber to our box size, we expect to achieve per cent accuracy at around $k \sim 20 h/\text{Mpc}$, in line with the result quoted in the paragraph above. We conclude that we have achieved the desired numerical convergence in the matter power spectrum, and as the main results of this work highlight, the impact of baryons on the total matter power spectrum exceeds the numerical accuracy at the scales of interest and depends on the exact implementation of baryonic physics (Figure 6).